

Characteristics of MHD Oscillations Observed with MDI

A. A. Norton¹ and R. K. Ulrich

Department of Physics and Astronomy, University of California,
Los Angeles, CA 90095

R. I. Bush

W.W. Hansen Experimental Physics Laboratory, Center for Space Science and
Astrophysics, Stanford University, Stanford, CA 94305

T. D. Tarbell

Lockheed Martin Research Laboratory, Palo Alto, CA 94304

Received _____; accepted _____

¹Visiting Scholar, Physics Department, Univ. of Queensland, Brisbane, QLD 4072
Australia

ABSTRACT

We report on the spatial distribution of magnetogram oscillatory power and phase angles between velocity and magnetogram signals as observed with the Michelson Doppler Imager. The dataset is $151.25'' \times 151.25''$ containing sunspot from Dec 2, 1997 with a temporal sampling interval of 60 seconds and spatial sampling of $0.605''$. Simultaneously observed continuum intensity and surface velocity accompany the magnetic information. We focus on three frequency regimes: 0.5-1.0, 3.0-3.5 and 5.5-6.0 mHz corresponding roughly to timescales of magnetic evolution, p -modes and the 3 minute resonant sunspot oscillation. Significant low frequency magnetogram power is found in lower flux pixels, 100-300 Gauss, in a striking ring with filamentary structure surrounding sunspot. Five minute magnetogram power peaks in extended regions of flux 600-800 Gauss. The 3 minute oscillation is observed in sunspot umbra in pixels whose flux measures 1300-1500 Gauss. Phase angles of approximately -90° between velocity and magnetic flux in the 3.0-3.5 and 5.5-6.0 mHz regimes are found in regions of significant cross amplitude.

Subject headings: MHD — Sun: magnetic fields — Sun: oscillations

1. Introduction

The interactions of photospheric magnetic fields with motions of solar plasma is described by magnetohydrodynamics (MHD). Ionson (1978) recognized that acoustic waves perturbing the base of magnetic fields can generate MHD waves. Significant amounts of literature exist addressing theoretical generation and propagation of MHD modes in the solar atmosphere. Previous identification of oscillatory modes in sunspots from velocity and intensity measurements is not sufficient since MHD modes require simultaneous magnetic field and velocity information. Observational support of solar MHD modes is sparse (Ulrich 1996, Horn et al., 1997, Norton et al., 1997, Lites et al., 1998, Rüedi et al., 1998).

Although many MHD waves may exist, two main mechanisms alter measured magnetic flux: 1) bending of field lines and 2) compression of field lines. Under simplified conditions, the bending mode corresponds to an Alfvén wave and a compressional mode corresponds to a magnetoacoustic wave. The observational tendency to image active regions at disk center may have historically hindered Alfvén wave detection. Measurement of δB due to a change in direction is easier to detect in transverse fields than in line-of-sight fields. It is easier to detect bending modes at the limb and compressional modes at disk center.

MHD waves are a prime coronal heating candidate. Suggested MHD wave dissipation processes are phase-mixing (Haeyvaerts and Priest 1983) and resonant absorption (Davila 1987). Detection of MHD oscillations is the first step towards understanding the role MHD waves play in atmospheric energy transport.

2. Observations

The MDI instrument images the sun at five different wavelengths centered around the mid-photospheric Ni-1 6768 Å line. Obtaining filtergrams at the five wavelengths samples

the line profile. The average of the left (LCP) and right circular polarized (RCP) observed central wavelengths is the Doppler shift. A longitudinal magnetic flux indicator, uncorrected for observation angle, is measured by subtracting the observed central wavelengths of RCP from LCP images. The continuum intensity is measured at a wavelength far from line center. We analyze a $151.25'' \times 151.25''$ sunspot centered region in the high resolution field on Dec 2, 1997. The dataset consists of 492 B, I_c and v images, snapshots shown in lower panels of Fig 1. The region is tracked by adjusting heliographic coordinates of map centers as a function of time. The average center to limb angle of the sunspot center is 19.77° . The data is stored as 3-D datacubes, sides of 250×250 pixels \times 492 minutes.

3. Analysis and Results

Temporal variations from individual pixels are analyzed without spatial averaging. Signals are detrended using a Gaussian filter (30 min width) before average values are subtracted. Power spectra of the signals are computed. 3-D datacubes are created where the temporal axis has been transformed into frequency. Averaging over the selected frequencies, we plot the spatial distribution of power for B, I_c and v in Fig 1. Magnetogram power plotted in Fig 1 is normalized so that the noise, as measured in the 7.5-8.0 mHz high frequency band, is unity. High frequency power in the strongest magnetic flux regions is enhanced by instrumental effects due to reduced intensity and broader absorption lines or by increased solar variations. We cannot distinguish between these options but if the high frequency power for these pixels is solar, our normalization could be incorrect.

Averaged magnetogram power spectra are plotted in Fig 2. Each signal is divided by its standard deviation. Then 399 spectra from pixels whose absolute mean measured flux is within 100-300, 600-800 and 1300-1500 G ranges are averaged and plotted in Fig 2. The ranges are selected because low frequency, p -mode and 3 minute power peaked herein.

Cross amplitude and phase spectra for the selected frequency regimes are found in Fig 3. To compute the cross spectra, signals are interpolated onto a ten second grid and shifted past each other in ten second lag increments up to a ± 15.16 minute period. The resulting cross covariance function is recorded. Restricting the lag interval to ensure wave train coherence time is equivalent to applying a Bartlett window. The Fourier transform of the cross covariance function, the cross spectrum, is computed at each position. Cross amplitude and phase spectra are plotted in the left and right columns of Fig 3, respectively.

4. Spurious Contributions to Oscillatory Magnetic Signal

Attention is given to two effects that could mimic an oscillatory magnetic signal: 1) misregistration of the LCP and RCP images and 2) optical depth changes due to temperature fluctuations affecting the measurement height where magnetic field gradients, dB/dz , are present. To determine whether magnetogram oscillations have their origin in LCP-RCP image differences, misregistered datasets were simulated. The details of this analysis will follow in a subsequent publication. Let it suffice herein to note that spurious contributions due to misregistered images are most worrisome in quiet regions. In active regions, the suppression of v amplitudes decreases the crosstalk between the v and B signals.

Opacity changes due to temperature fluctuations can not be ruled out as a source of spurious oscillatory magnetic signal without an indicator such as thermal line ratios. The analysis of MDI flux estimates as a function of temperature will be presented in a subsequent publication. We acknowledge that crosstalk into the δB signal from fluctuations in temperature, density and other parameters may contribute to magnetogram oscillations measured herein. Further research will determine what, if any, corrections are necessary to convert magnetogram variation into a measure of magnetic field strength variation.

5. Discussion

Most significantly, spatial distribution of magnetogram power is distinctly different in the three frequency regimes. Low frequency buffeting and evolution occurs around sunspot and plage. Notable filamentary structure seen across the penumbra/quiet boundary intimates an advection of flux at low frequencies. Magnetogram oscillations on the 5 minute timescale are presumably the magnetic response to velocities already present in the photosphere. Five minute magnetogram oscillations in extended plage regions suggest the plage environment may more readily convert acoustic waves into MHD waves. The 3 minute resonant sunspot oscillation is found in a portion of the umbra not associated with the strongest flux, but rather an area bounding the darkest part of the umbra.

The uneven spatial distribution of power would cause an investigation restricting its MHD wave search to the strongest flux areas to be unsuccessful. It is not yet clear what conditions are favorable for the generation of measurable MHD oscillations. Loop termination points or strong gradients in magnetic fields might be required. The power distribution and small scale nature of the magnetic element does not lend itself to spatial averaging. The power spectra shape seen in Fig 2 becomes flatter with increasing flux. Stronger fields evolve less, leveling the spectra at low frequency. The increase of high frequency power in strong flux spectra is due to reduced intensity and broader absorption lines or by increased solar variation. The changing shape of magnetogram spectra should be taken into account when comparing power from regions of differing B values.

Some positions containing strong magnetic power at 3.0-3.5 mHz in Fig 1 do not show correspondingly high $(v, \delta|B|)$ cross amplitude values in Fig 3. This suggests the presence of different MHD modes or crosstalk mechanisms. The mode with stronger line-of-sight velocity variations is more visible in the cross amplitude plot.

Phase angles of approximately -90° between $(v, \delta|B|)$ can be interpreted as $\delta|B|$

reaching its maximum a quarter of a cycle before v . Phases of -90° dominate regions of significant cross amplitude in the 5 and 3 minute bands. This phase relation is not a measure of magnetoacoustic waves in which v is expected to lead $\delta|B|$. Its interpretation is still uncertain, but Rüedi et al (1999) demonstrates that $\delta|B|$ leading v a quarter of a cycle could be the result of measuring dB/dz during opacity changes. It appears that at least three different mechanisms (crosstalk or other) dominate at different spatial positions, producing the phase structure seen in Fig 3. We will not know how the observational bias against detecting Alfvén waves at disk-center affects phase determinations until a similar analysis can be conducted with limb data for comparison. Phase relations described by Ulrich (1996) may not apply in sunspots where the fluxtube model is inappropriate.

Temperature, density and corresponding opacity variations may contribute to B amplitudes and phases through crosstalk. Although the interpretation of the signal variation is complicated by the effects of crosstalk, the crosstalk is nonetheless of solar origin so that the spectral power density maps provide a real measure of MHD oscillations. The distinct spatial distribution of magnetogram power in the three frequency regimes can assist in region selection of future MHD wave searches as well as numerical comparison of amplitude and phase measurements from other datasets.

REFERENCES

- Davila, J. M., 1987, ApJ, 317, 514
- Heyvaerts, J. & Priest, E. R., 1983, A&A, 318, 957
- Horn, T., Staude, J. and Landgraf, V., 1997, Sol Phys 172, 69
- Ionson, J. A., 1978, ApJ, 226, 650
- Lites, B. W., Thomas, J. H., Bogdan, T. J., and Cally, P. S., ApJ, 497, 464.
- Norton, A. A., Ulrich, R. K., Bogart, R. S., Bush, R. I, and Hoeksema, J. T., 1998, in: *New Eyes to See Inside the Sun and Stars*, Deubner, F.-L., Christensen-Daalsgaard, J., Kurtz, D. (Eds.) , IAU Symp 185, 453
- Rüedi, I., Solanki, S. K, Stenflo, J. O., Tarbell, T., and Scherrer, P. H., 1998, A&A, 335, L97-L100
- Rüedi, I., Solanki, S. K, Bogdan, T., and Cally, P. 1999, in: *Solar Polarization*, Proc. 2nd Solar Polarization Workshop, Nagendra, K. N. and Stenflo, J. O. (Eds.), in press
- Ulrich, R. K., 1996, ApJ, 465, 436

Fig. 1.— Context images and spatial distributions of power are shown. Rows from bottom: context images, 0.5-1.0, 3.0-3.5 and 5.5-6.0 mHz frequencies. Columns from left contain B, I_c and v data. Grayscales: black-max, white-min except the I_c context image is reversed. Context images from left to right have maximum values of 2057 G, 3436, 1.3 km/s and minimum values of -876 G, 658, -1.3 km/s. The maximum values of power from lower to upper plots are B: 1000, 220, 178 normalized power units, I_c : 10445, 1690, 280, and v : 53×10^3 , 151×10^3 , 10×10^3 (m/s)². Minimum power values are B: 7.2, 8.4, 6.9 normalized power units, I_c : 10, 3.2, 2.2, and v : 153, 1650, 70 (m/s)².

Fig. 2.— The logarithm of rms normalized magnetic power is plotted as a function of frequency for pixels whose mean flux values are within the 100-300, 600-800 and 1300-1500 Gauss ranges. The average standard deviation values used for signal normalization are 13.0, 14.3, 15.9 G, respectively.

Fig. 3.— Cross amplitude (left) and phase spectra (right) is shown for the 0.5-1.0, 3.0-3.5 and 5.5-6.0 mHz regimes. Phase data is plotted for all spatial points, regardless of cross amplitude significance, in order to display spatial structure of phases.

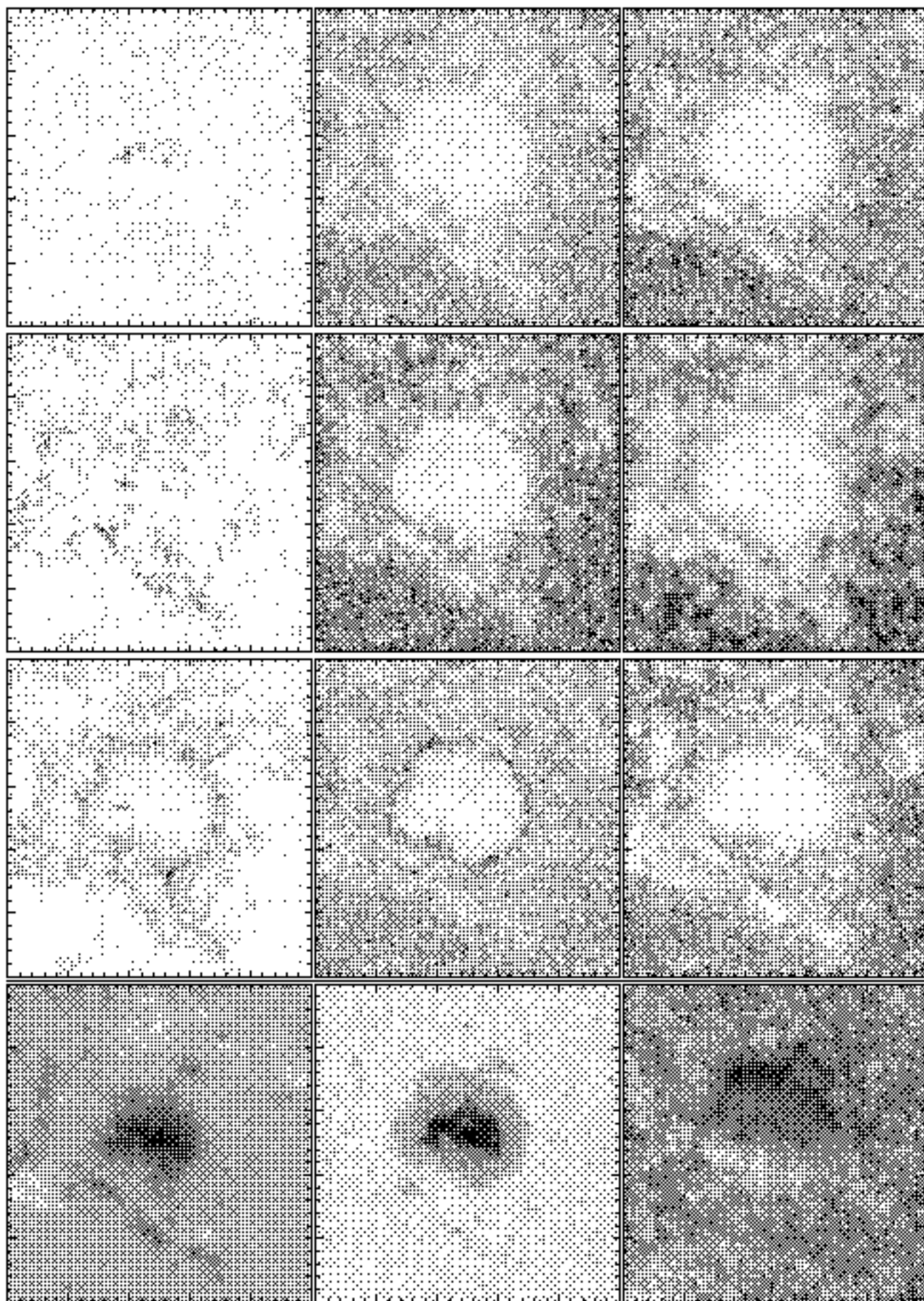
$\langle \delta B \rangle^2$, normalized $\langle \delta I_0 \rangle^2$ $\langle \delta V \rangle^2$

5.5 – 6.0 mHz

3.0 – 3.5 mHz

0.5 – 1.0 mHz

Context Images



Magnetogram

Continuum Intensity

Doppler Velocity

100–300 G

600–800 G

1300–1500 G

